ACS APPLIED MATERIALS & INTERFACES

www.acsami.org

Research Article

Evidence of Mn-Ion Structural Displacements Correlated with Oxygen Vacancies in $La_{0.7}Sr_{0.3}MnO_3$ Interfacial Dead Layers

Piu Rajak,* Daniel Knez, Sandeep Kumar Chaluvadi, Pasquale Orgiani, Giorgio Rossi, Laurence Méchin, and Regina Ciancio*

Cite This: *ACS Appl. Mater. Interfaces* 2021, 13, 55666–55675

Read Online

ACCESS | Metrics & More | Article Recommendations | Supporting Information

ABSTRACT: The properties of half-metallic manganite thin films depend on the composition and structure in the atomic scale, and consequently, their potential functional behavior can only be based on fine structure characterization. By combining advanced transmission electron microscopy, electron energy loss spectroscopy, density functional theory calculations, and multislice image simulations, we obtained evidence of a 7 nm-thick interface layer in $La_{0.7}Sr_{0.3}MnO_3$ (LSMO) thin films, compatible with the formation of well-known dead layers in manganites, with an elongated out-of-plane lattice parameter and structural and electronic properties well distinguished from the bulk of the film. We observed, for the first time, a structural shift of Mn ions coupled with oxygen vacancies and a reduced Mn valence state within such layer. Understanding the correlation between oxygen vacancies, the Mn oxidation state, and Mn-ion displacements is a prerequisite to engineer the magnetotransport properties of LSMO thin films.

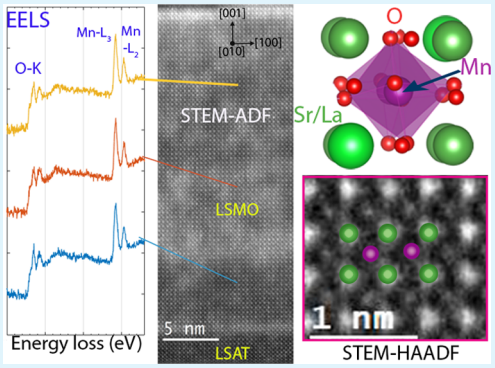

KEYWORDS: *aberration-corrected scanning transmission electron microscopy, dead layer, EELS and EDS, oxygen vacancy, density functional theory (DFT), multislice image simulation*

1. INTRODUCTION

Transition metal oxides with perovskite structures (ABO_3) are fascinating systems that host a vast array of unique phenomena, such as high-temperature (and unconventional) superconductivity, colossal magnetoresistance,[1,2] all forms of magnetic and ferroelectric order parameters, and the interplay between these phases. The recent years have witnessed an increasing ability to grow thin-film heterostructures of these materials with atomic precision. With this level of control, the electrostatic boundary conditions at oxide surfaces and interfaces can be used to form new electronic configurations as a consequence of epitaxial strain, orbital hybridization, and reduced dimensionality. Notably, colossal magnetoresistive manganite films with the composition $La_{0.7}Sr_{0.3}MnO_3$ (LSMO) are of great interest because of their half-metallicity, room-temperature ferromagnetism, and the competition between lattice, spin, and charge degrees of freedom[3−9] that create an ideal platform for exploring oxide spintronic applications. Although bulk LSMO is a metallic ferromagnet, it is well known that LSMO ultrathin films become insulators with a greatly reduced magnetization when their thickness is less than a critical value of 4 unit cells.[10,11] The layer characterized by suppressed magnetization and metallicity is commonly called "dead layer".[12,13] Many mechanisms have been proposed to explain the formation of magnetic dead layers at interfaces, including cation intermixing,[14] strain-induced spin canting,[15] interfacial orbital reconstruction,[16] oxygen octahedral rotation,[17,18] and polar discontinuity across the interfaces.[19−23] The latter yields an uncompensated extra charge that can drive a potential divergence, that is, polar catastrophe, which affects the stoichiometry of manganites at the interface. In spite of abundant investigation, the origin of a magnetic dead layer at the LSMO/substrate interface is still not well understood. From the structural point of view, bulk LSMO (A site: La and Sr, B site: Mn) has rhombohedral symmetry with the space group $R\bar{3}C$ and the $a-a-a-$ Glazer notation,[24] revealing equal and out-of-plane BO_6 octahedral tilting in all three directions. Several studies have evidenced that not only the dead layer thickness but also the magnetic properties of epitaxially grown LSMO oxides can be tuned by controlling the oxygen coordination,[25] interfacial oxygen octahedral rotation,[18] interfacial strain,[26,27] and concentration of oxygen defects.[27]

In previous studies, scanning transmission electron microscopy (STEM) and electron energy loss spectroscopy (EELS) have proven effective in examining structures and cation charge

Received: August 16, 2021
Accepted: October 12, 2021
Published: November 11, 2021

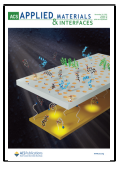

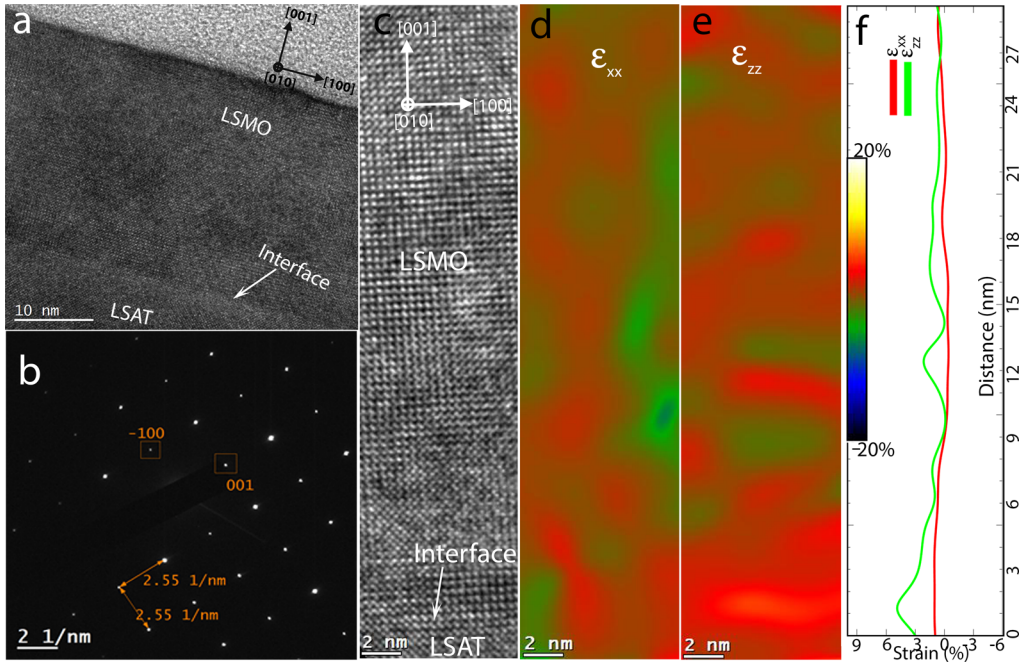

Figure 1. Cross-sectional HRTEM image and corresponding strain analysis: (a) HRTEM image of the [001]-oriented LSMO thin film grown on the LSAT substrate, (b) SAED pattern from the imaged region, (c) experimental HRTEM image used for strain analysis, and (d,e) symmetric strain components: in-plane (ε_{xx}) and out-of-plane (ε_{zz}) respectively. A color bar for the strain map is shown. (f) Line profiles of the strain components, averaged over the width of the strain maps in the [100] direction of the film. All strain values indicated in this figure are in percentage.

states in thin films. For EELS, fine spectral features from the cation and oxygen edges, energy onset, and intensity ratio of the core-loss edges can be used to quantify B-site charge states as well as to determine the film stoichiometry.[14,28−35]

Here, we provide the first evidence of Mn-ion (B-site) displacement correlated with the reduction of the Mn valence state in the neighborhood of the film/substrate interface in LSMO thin films as grown on (001)-oriented $(LaAlO_3)_{0.3}$−$(Sr_2AlTaO_6)_{0.7}$ (henceforth LSAT) substrates by means of pulsed laser deposition (PLD). First, we assess the quality and strain properties of the LSMO/LSAT heterostructure by high-resolution TEM (HRTEM) and geometrical phase analysis (GPA).[36] By using aberration-corrected STEM imaging with a high-angle annular dark-field (HAADF) detector and a low-angle annular dark-field (ADF) detector, EELS, atomistic calculations, and STEM image simulations, we correlate the observed Mn displacements with the changes in the valence state of Mn ions from its optimal value of 3.3, as well as with oxygen vacancies, throughout the film. In particular, STEM−ADF imaging shows enhanced defect contrast in the presence of oxygen vacancies, providing direct evidence of the formation of a 7 nm-thick interfacial region in the LSMO film that is structurally different from the bulk of the film and can be associated with the magnetic dead layer of manganites. EELS analysis indicates a preferential formation of oxygen vacancies in LSMO at the interfacial region with the substrate with respect to the rest of the film, which is accompanied by an out-of-plane lattice expansion. By comparing the STEM results and multislice simulations based on test structures as obtained from density functional theory (DFT) calculations, we probe the formation of an oxygen-deficient structure with displaced Mn ions and discuss the origin of the dead layer as consequent to the lattice strain and Mn-ion displacements.

2. EXPERIMENTAL AND CALCULATION DETAILS

2.1. Thin-Film Fabrication. Epitaxial LSMO thin films were grown on cubic LSAT (001) substrates by PLD using a KrF excimer laser (248 nm, repetition rate 3 Hz, fluence of 1.4−2 J/cm^2). The choice of LSAT substrate is driven by its great thermal stability and low lattice mismatch with the film (0.2%). The substrate temperature and oxygen partial pressure (PO_2) during deposition were maintained at 720 °C and 0.35 mbar, respectively. After deposition, the films were cooled down to room temperature at a rate of 15 °C/min in 700 mbar O_2 pressure.[37] Detailed structural characterizations (θ−2θ, reciprocal space maps, ω, and ϕ-scans) were performed by PANalytical X'Pert four-circle X-ray diffraction (XRD) and morphological characterizations by atomic force microscopy (AFM).

2.2. TEM Imaging and Spectroscopy. Cross-sectional TEM samples were prepared using the conventional sandwich technique. At first, the samples were mechanically ground, then dimpled and, eventually, thinned down to electron transperancy by Ar^+ ion beam milling.

The HRTEM investigations were performed by using the JEOL 2010 UHR field emission gun microscope operated at 200 kV with a measured spherical aberration coefficient C_s of 0.47 ± 0.01. In all cases, the sample was tilted to [010] zone axes, aligning the film growth direction of the heterostructure perpendicular to the electron beam direction.

High-resolution STEM (HRSTEM) were performed on a probe-corrected FEI Titan^3 G2 60-300 operating at 300 keV with a convergence angle of 19.6 mrad. A Gatan Quantum energy filter (GIF) and a four-quadrant Super-X detector (FEI) were used for EELS and EDX spectrum acquisition, respectively. Simultaneously, HAADF and ADF image acquisition was performed. The inner and outer detection angles of the HAADF detector were 116.7 and 177 and 24.1 and 55 mrad for the ADF detector, respectively. The collection semiangle and dispersion channel width of EELS acquisition were 24.59 mrad and 0.25 eV, respectively. To correct the intrinsic shift of energy of the electron beam, the zero-loss peak was used, which was recorded simultaneously using the Dual EELS mode of the spectrometer. The sample was oriented to the [010] axis

https://doi.org/10.1021/acsami.1c15599
ACS Appl. Mater. Interfaces 2021, 13, 55666−55675

of the LSMO thin films and the fast scanning direction was oriented perpendicular to the interface.

2.3. Data Evaluation. Gatan Digital Micrograph 3.13 (GMS 3.13) was used to process EELS and EDX data. For EELS quantification, at first, the raw EELS data sets were background-corrected using a pre-edge power law fit, and plural scattering was removed via zero-loss deconvolution.[38] The absolute energy onset was calibrated carefully with the simultaneously acquired zero-loss peak. Then, the valence state of Mn was determined by the energy difference between the pre-peak and the main peak of the O−K edges as described by Varela et al.[30] To compare all experimental techniques reliably and quantitatively, the atomic column positions have been extracted, and the displacements of the cations were quantified by using the StatSTEM software.[39]

GPA developed by Hÿtch et al.[36] was used to measure the strain within the film region using an HRTEM image. Strain map calculation was carried out with scripts in the FRWR tools menu (FRWR, 2012)[40] for Gatan Digital Micrograph software. Two [200] and [002] Bragg spots were used to calculate two-dimensional symmetric strain components. Depending on the aperture size used for the Bragg spots, the spatial sampling of strain measurement was 3 nm.

2.4. DFT Calculations. In order to confirm experimental observation theoretically, the LSMO supercell was relaxed with first-principles methods. DFT calculations have been performed using the Quantum Espresso[41] code using the Perdew−Burke−Ernzerhof (PBE) exchange−correlation functional[42] and ultrasoft pseudopotentials.[43] Semicore 3s and 3p states were included in the valence electron configuration for the Mn atom (for La, Mn, and O atoms, the valence electron configuration of $5s^2 5p^6 6s^2 5d^1$, $3s^2 3p^6 3d^5 4s^2$, and $2s^2 2p^4$, respectively). The cutoff for the plane-wave wave functions and the kinetic energy were set as 50 and 450 Ry, respectively. The atomic positions and the free lattice parameters were relaxed using the BFGS (Broyden−Fletcher−Goldfarb−Shanno) algorithm until the forces on the atoms were below 1 meV/Å for the bulk and strain calculations.

2.5. STEM−HAADF Image Simulation. The STEM−HAADF images were simulated using a multislice algorithm with Frozen Phonon approximation to allow quantitative comparison with experimental micrographs. The simulations were executed using QSTEM,[40] with parameters as of the experiment: 300 kV acceleration voltage, 19.6 mrad convergence angle, 5 μm Cs, 0.8 eV energy spread (dE), and −3.8 nm defocus with a total of 15 phonon configurations. For simulation, the LSMO structure was oriented along the viewing direction [010] as of experiment with a thickness of 50 nm along the electron beam direction. To perform a multislice algorithm, the slice thickness of the LSMO structure was chosen 1.99 Å. The scan areas were 110 Å × 110 Å, which sampled by 220 × 220 pixels. The probe array and resolution were kept as 400 × 400 pixel and 0.037 × 0.037 Å, respectively.

3. RESULTS AND DISCUSSION

Figure 1a displays a representative cross-sectional HRTEM image of the LSMO/LSAT heterostructure taken in the [010] zone axis, showing that the LSMO films have a good crystalline quality as well as smooth and atomically flat interfaces with the substrate. The corresponding selected area electron diffraction (SAED) pattern shown in Figure 1b enlightens the very good crystalline matching between the LSMO film and the LSAT substrate with the LSMO (001)||LSAT (001) epitaxial relationship.

The quality and the strain distribution of the film were further explored by GPA.[36] The in-plane strain map ε_{xx} [where $\varepsilon_{xx} = (a_{LSMO} - a_{LSAT})/a_{LSAT}$, with a_{LSMO} and a_{LSAT} being the in-plane lattice parameters of LSMO and LSAT, respectively] and the out-of-plane strain maps ε_{zz} [where $\varepsilon_{zz} = (c_{LSMO} - c_{LSAT})/c_{LSAT}$, where c_{LSMO} and c_{LSAT} being the out-of-plane lattice parameters of LSMO and LSAT, respectively), as calculated from Figure 1c by keeping the LSAT substrate as a reference, are presented in Figure 1d,e, respectively. The integrated line profile of the strain distribution shown in Figure 1f provides evidence of minor strain variations of ε_{xx} in the rest of the film (i.e., beyond 7 nm), as expected for epitaxial growth. Moreover, the film grows perfectly coherent in-plane, with almost the same lattice parameter of the LSAT substrate (a_{LSAT} = 3.868 Å[44]). Remarkably, in Figure 1f, an increase of the out-of-plane strain with a value of +2.4 ± 0.5% is measured over the first 7 nm of the film relative to LSAT, which corresponds to an out-of-plane lattice parameter ≈ 3.960 Å, that is, +2.1% compared to bulk LSMO (a_{bulk} = 3.876 Å[45]). The ε_{zz} value for the rest of the LSMO film (beyond 7 nm) is approximately +0.8 ± 0.3%, which corresponds to the out-of-plane lattice parameter of 3.898 Å.

The presence of out-of-plane strain gradients in the absence of dislocations or crystal twinning indicates an interesting strain relief mechanism. It is worth mentioning that in perovskite systems, the epitaxial strain is accommodated mainly by changes in the lattice constants or by structural distortions such as changing bond lengths or octahedral tilting.[46,47]

To elucidate the origin of the strain distribution in the LSMO/LSAT heterostructure, we performed aberration-corrected STEM with HA/ADF detectors. A representative cross-sectional STEM−HAADF image of the LSMO/LSAT heterostructure shown in Figure 2a reveals that the film has a

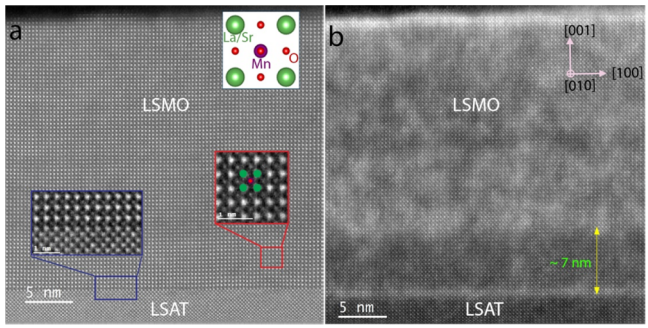

Figure 2. Experimental high-resolution STEM images. (a) STEM−HAADF image showing the cross-sectional geometry of the LSMO/LSAT heterostructure along the [010] zone axis. The inset in the blue box shows that the interface is atomically flat and defect free. The inset in the red box shows a close-up image of the LSMO thin film. The scale bar of the insets corresponds to 1 nm. The upper right inset shows the projection of the LSMO unit cell along the [010] direction where green, purple, and red-colored circles represent La/Sr, Mn, and O atomic column positions, respectively. (b) STEM−ADF image showing the contrast variation at around 7 nm distance from the interface.

uniform structure and the interface is atomically sharp with no visible defects (a magnified image is shown in the blue-colored box) nor cation interdiffusion between the LSAT substrate and the LSMO film (t/λ profiles are given in Figure S1 in the Supporting Information). Considering that STEM−HAADF experiments produce images whose contrast is approximately proportional to the square of the average atomic number,[48,49] in Figure 2a, La/Sr atomic columns have brighter contrast (marked with a green circle in the inset), while darker contrast is associated with Mn positions (a magnified image is shown in the inset with a red-colored box superimposed to the image with La/Sr and Mn columns labeled in green and purple, respectively). As the presence of oxygen vacancies is better

https://doi.org/10.1021/acsami.1c15599
ACS Appl. Mater. Interfaces 2021, 13, 55666−55675

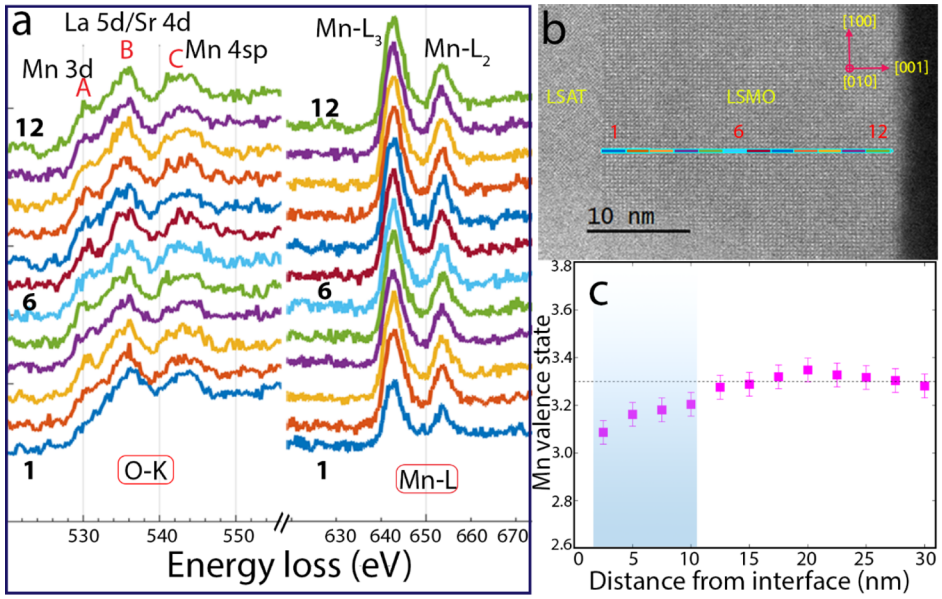

Figure 3. EELS analysis of the Mn oxidation state in the film region. (a) Fine structures of O−K and Mn-L edges. Three prominent peaks for O−K edges are labeled "A", "B", and "C". Peaks "A" and "C" correspond to O 2p−Mn 3d and 4sp hybrid states, respectively, while peak "B" is characteristic of O 2p Sr 4d or La 5d hybrid states. The energy difference ΔE between peaks "A" and "B" was measured to determine the Mn valency. (b) STEM−HAADF image of the LSMO/LSAT structure and the line shows the area from where EELS line profiles have been collected. The numbers indicate the area across which the average spectra were collected. (c) Estimated Mn valence in the LSMO film as a function of distance from the interface with the substrate.

emphasized by ADF,[50,51] we compare the HAADF and ADF signals of the same region.

Figure 2b shows a STEM−ADF image of the heterostructure acquired simultaneously with Figure 2a. Contrast variations can be appreciated within the film and observed to recur at measurable distances from the interface. In particular, a well-defined darker contrast layer of about 7 nm thickness is observed in the LSMO film at the interface with the substrate, which recalls the typical values of dead layers[52] in LSMO thin films. Differently from HAADF, the ADF signal is known to be very sensitive to the dechanneling of the incident electron beam caused by defects such as vacancies and lattice distortion around vacancy sites, as well as strain surrounding the defects.[50,53−57] Based on the experimental evidence, the presence of contrast variations throughout the film can be attributed to a different concentration of oxygen vacancies, with a distinct darker contrast in the first 7 nm interfacial region of the LSMO film where on average, a higher strain value is also measured (Figure 1f). To validate this, the out-of-plane (ϵ_{zz}) strain was also calculated from HAADF−STEM (presented in Figure S2 in the Supporting Information), and it also confirms the presence of higher strain values at the 7 nm interfacial region.

Energy-dispersive X-ray spectroscopy (EDXS) elemental mapping performed at the film/substrate interface further supports our interpretation of the STEM−HAADF results, ruling out the possibility of cation interdiffusion from the LSAT substrate to the LSMO film (see Figure S2 in the Supporting Information).

To obtain quantitative information on the oxygen distribution, we probe the local Mn valence[30] changes by performing site-selective EELS across the film thickness. The EELS line scans shown in Figure 3a highlight the changes in the fine structure of the O K and Mn $L_{2,3}$ edge spectra from the interface to the surface. Twelve spectra were collected from the interface to the LSMO film surface, each one averaging over 2.5 nm along the [001] direction and 4.85 nm along the [100] direction of the film. In Figure 3b, the regions from which spectra were collected are numbered from 1 to 12, while in Figure 3a, all the corresponding 12 spectra are stacked vertically for ease of visualization. To determine the valence state of the Mn atoms, electron energy-loss near-edge structures of O K-edges have been used. The fine structure of the O K edge provides information on the electronic excitation from O 1s to 2p bands. The three main peaks of the O K edges are labeled "A", "B", and "C" in Figure 3a. It can be noted that peak "A" intensities change when moving from the interface to the surface of the film. The weakening of peaks "A" and "C" in conjunction with the broadening of main peak "B" has been recognized as the signature of the presence of oxygen vacancies.[58] Besides, the energy difference between peak "A" and peak "B" also increases steadily with distance from the interface. The change in the Mn valence state (details are in the Supporting Information) over the film region is summarized in Figure 3c. The nominal Mn valence of bulk LSMO (marked as a dashed line in Figure 3c) is 3.3. The Mn valence state increases gradually from approximately +3.1 ± 0.05 to +3.3 ± 0.05 toward the surface of the film, which reveals that the concentration of oxygen vacancies increases (Mn valence decreases) when nearing the interface with the substrate. As a matter of fact, the term "dead layer" indicates the interfacial region with depressed electric and magnetic properties, corresponding to the Mn valence value smaller than 3.3. Such a region is not fully insulating and antiferromagnetic since, according to the well-accepted manganite phase diagrams,[59,60] LSMO turns to be metallic when the Mn valence value is larger than 3.1, which occurs above 2 nm (i.e., 5 unit cells) from the interface with the substrate. Such a thickness is compatible with those reported in the literature for the insulating dead layer and with our best samples. The

https://doi.org/10.1021/acsami.1c15599
ACS Appl. Mater. Interfaces 2021, 13, 55666−55675

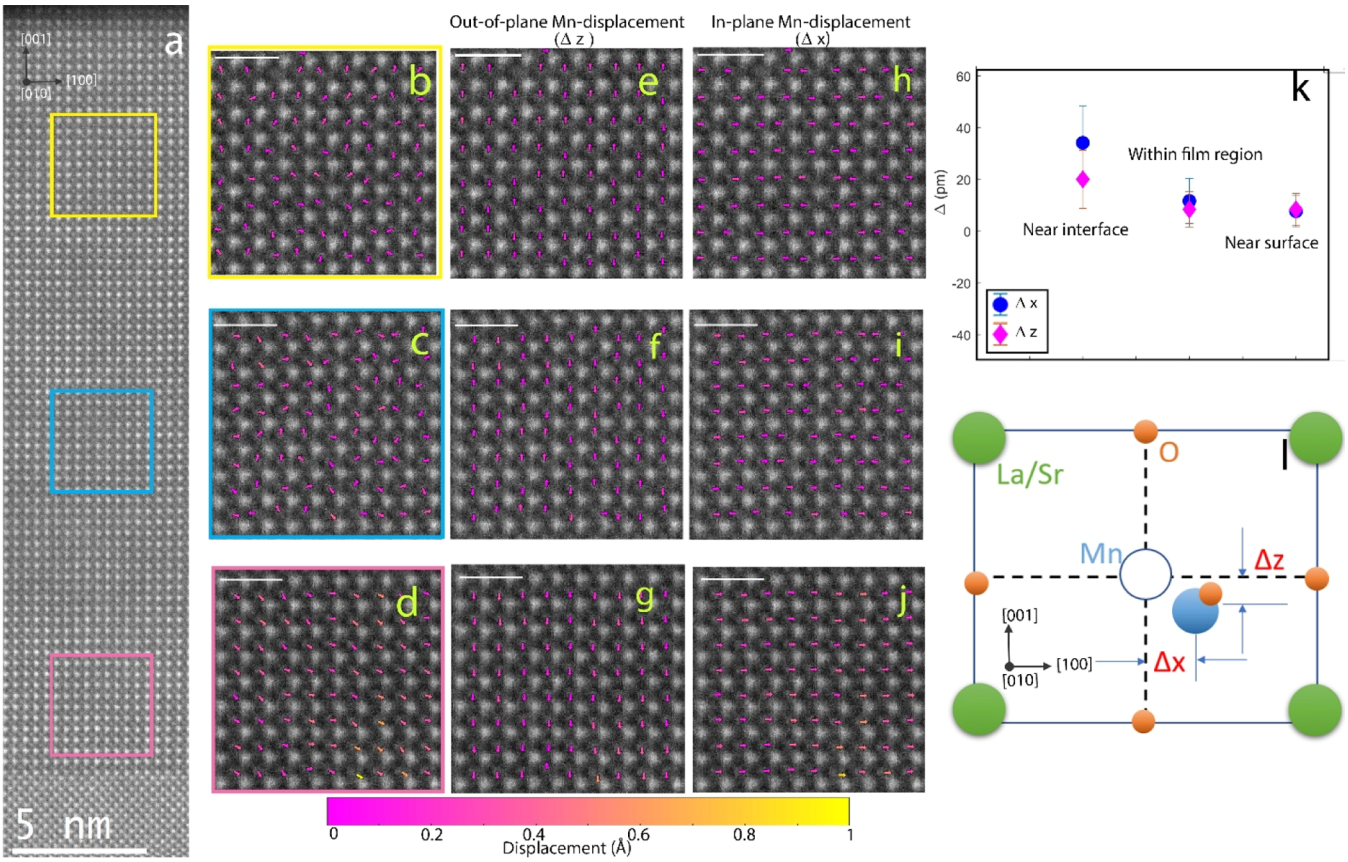

Figure 4. Quantitative analysis of the Mn-ion (B-site) displacements over the LSMO film. (a) Boxes marked in a different color on the STEM−HAADF image represent the regions used to map the displacement of Mn ions (B-site). (b−d) Map of atomic displacement vectors showing the displacement of Mn atoms (arrows) from the center of the projected La atoms superposed on the STEM−HAADF image [010] zone axis. (e−g) Out-of-plane (Δz) component and (h−j) in-plane (Δx) component of Mn displacements calculated from the corresponding regions. The scale bar on the images represents 1 nm. (k) Plot shows the variation in the magnitude of Δz and Δx from three different regions. (l) Projection of the LSMO unit cell along the [010] direction, where Δx and Δz denote the shift of Mn-ion (B-site) (blue) atoms along the in-plane and out-of-plane directions, respectively, concerning the centrosymmetric position (open circle).

reduction of the Mn oxidation state has also been observed in (La, Ca)MnO_3/STO_6,[61] $SrMnO_3$/LSAT,[44] and $TbMnO_3$/STO,[62] and it was proposed as a possible explanation of the observed magnetic dead layer in such systems.[12]

In addition, although the averaged values for the Mn valence state calculated from EELS spectra appear to slightly decrease when the film thickness reaches 20 nm, they still correspond to the optimal value of 3.3 within our experimental error, with no evidence of the presence of Mn^{2+} ions at the LSMO surface.[63] The slight decrease of the Mn valence state toward the surface can also be explained due to some extrinsic effects during TEM sample preparation.[64] Differently, the reduction of the Mn valence state in the proximity of the LSMO film/LSAT substrate interface is well above our experimental sensitivity.

The strain, the changes in the Mn valence state, and the variations in oxygen signal provide combined evidence of a deviation from the typical perovskite structure of LSMO in the proximity of the interface. The vacancies in ultrathin oxide films can form due to multiple reasons such as the interlayer effect,[65] chemical potential difference,[66] or during the growth stage of the LSMO film.[31] In our case, oxygen vacancies in the LSMO films cannot be attributed to any chemical effect since EDXS measurements do not show any cation inter-diffusion across the film/substrate interfaces (see Figure S3). On the other hand, similar to other oxide systems,[67] the Mn-ion displacements at the interface region suggest a possible role of residual strain in promoting oxygen vacancies at specific atomic sites. When oxygen vacancies are induced in LSMO, the charge compensating electrons localize on nearby Mn ions lowering their oxidation state (e.g., from Mn^{4+} to Mn^{3+}). We observe from the STEM−HAADF images, a collective displacement of Mn ions from their centrosymmetric positions. To obtain quantitative information about the distribution and arrangement of the lattice distortions, we took a closer look at the STEM−HAADF image in Figure 4 and identified the presence of regions with different Mn displacements.

The atomic positions are obtained precisely from the HAADF images by using a center-of-mass refinement approach with picometer resolution, as implemented with StatSTEM[39] software. The relative displacements of Mn ions (B-site) from centrosymmetric locations are measured using La ion (A-site) positions as a reference. A schematic of one projected unit cell of LSMO is provided in Figure 4l where the positions of Mn, La/Sr, and O atomic columns are labeled blue, green, and orange circles, respectively. The relative displacements of the Mn ions from the center of the pseudocubic perovskite cell along the **a** and **c** crystallographic directions are indicated by Δx and Δz, respectively (illustrated in Figure 4l). Three regions of the film are evaluated using this method (regions are marked in Figure 4a), and the results are displayed in Figure

https://doi.org/10.1021/acsami.1c15599
ACS Appl. Mater. Interfaces 2021, 13, 55666−55675

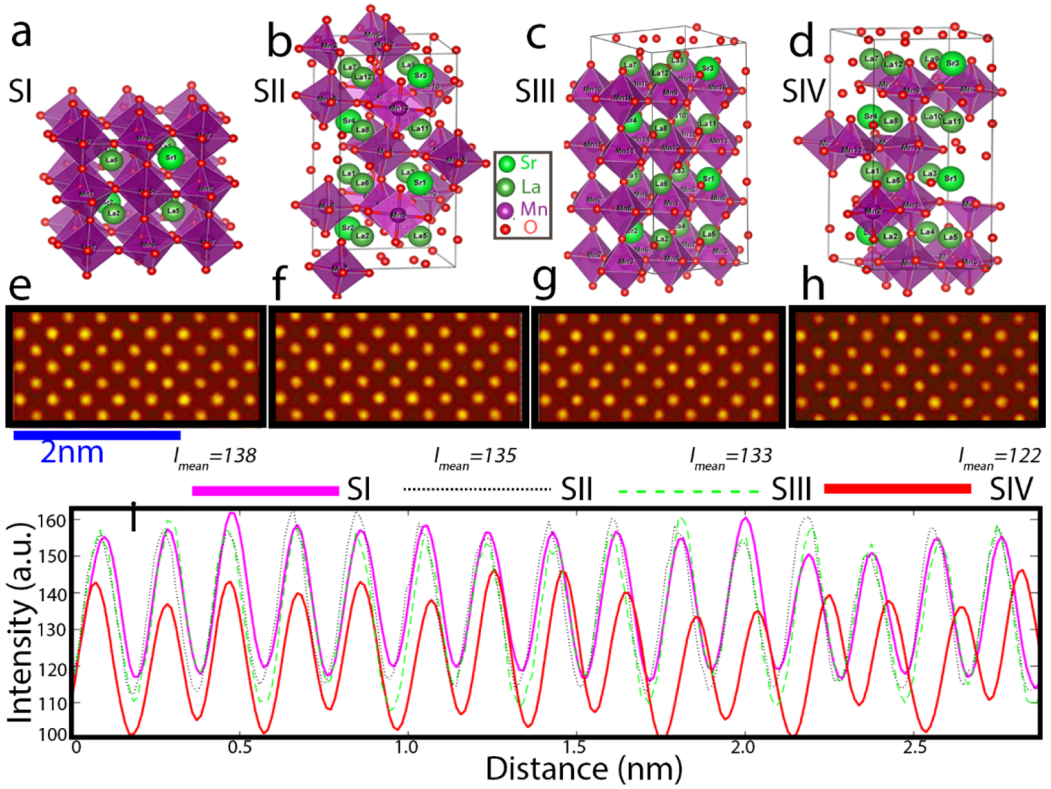

Figure 5. Atomistic simulation results. (a–d) Represent the 3D view of the energetically relaxed structures by DFT calculation for structures SI, SII, SIII, and SIV, respectively. The incomplete polyhedral shows the position of oxygen vacancies at the other end of the polyhedral (e–h) multislice simulated STEM–ADF images of the [010]-orientated LSMO structure with 15 nm thickness using the corresponding structures. The scale bar is the same for all the simulated images. (i) Intensity profile calculated from each simulated STEM–ADF image.

4b–d. The Mn-ion displacement map (Figure 4b–d) superimposed on the STEM–HAADF image shows the major alignment of Mn-ion displacements along the **a** axis. The corresponding out-of-plane (Δz) component of Mn-ion displacements of each region is presented in Figure 4e–f. Similarly, in Figure 4h–j, the in-plane (Δx) component of Mn-ion displacements is presented. The arrows indicate the direction of Mn-ion displacements relative to the center of La ions, and the corresponding color scale indicates the magnitude of the displacements. It can be noted that Mn-ion displacements near the surface region and in the middle of the LSMO film have random distribution, while an ordered displacement vectors can be measured at the region close to the interface. The Δz and Δx average magnitude values measured over each region are plotted in Figure 4k, which shows higher Δz and Δx values at the interfacial region compared to the rest of the film. The measured average value of Δz and Δx at the near-surface region of the LSMO film is 8 ± 6 pm, which can be attributed to some image distortions, including specimen drift, scanning noise.[68] By taking this value as a precision limit, the calculated average magnitude of the local Mn-ion displacement is $\Delta x = 26 \pm 10$ pm and $\Delta z = 10 \pm 10$ pm (see the Supporting Information) along the in-plane and out-of-plane direction. Interestingly, both the mean values of Δz and Δx reach their maximum off-center displacements close to the interface (Figure 4d,k), in the so-called dead layer region. This increase in the magnitude of the displacement of Mn ions is consistent with the increase in the population of oxygen vacancies at the dead layer of the LSMO film. It can be understood that the presence of oxygen vacancies generates locally additional positive charges, and the oxygen octahedron can be extended and rotated by applying the strain tensor to the oxygen vacancy. Even though intuitively an oxygen vacancy would isotropically affect the nearest Mn ions (i.e., moving them away from the vacancy position),[69] surprisingly STEM–HAADF analyses are conclusive in detecting a coherent displacement of Mn ions in one specific direction. The origin of unidirectional displacement will be the subject of more focused work. The structural modifications exemplified by the Mn-ion displacements accompanied by the presence of localized formation of oxygen vacancies at the interface region suggest a crucial role of possible residual strain effects in promoting oxygen vacancies, as also observed in other oxide systems such as CeO_2.[67] This finding is in strong agreement with the above strain analysis, which shows that the out-of-plane strain near the interface is higher than in the remaining part of the LSMO thin film.

DFT modeling and multislice calculations were used to evaluate the impact of lattice distortions and atomic displacement in the presence of oxygen vacancies. Details of the calculation parameters are given in the Experimental and Calculation Details section. To this end, we examined four different test structures (presented in Figure 5a–d): (i) bulk LSMO unit cell (hereafter SI), (ii) supercell with oxygen vacancies (henceforth SII), (iii) supercell with a displacement of Mn ions from B-site (hereafter SIII), and (iv) supercell with oxygen vacancies and Mn-ion (B-site) displacement (onward SIV). Oxygen vacancies were generated randomly in these test structures. Structures SI, SII, and SIV were energetically relaxed by DFT calculations, and structure SIII was built from SI by introducing additional displacements to the Mn ions along the [110] direction by 29 pm (roughly equivalent to the

https://doi.org/10.1021/acsami.1c15599
ACS Appl. Mater. Interfaces 2021, 13, 55666–55675

corresponding displacements resulting from the experimental data). More details of the structural models and simulation parameters are given in the Supporting Information. The energetically relaxed structures show atomic rearrangements due to the presence of vacancies and Mn-ion displacements, which may contribute to the observed STEM contrast.

Finally, based on the relaxed structures, multislice image simulations were performed to better visualize the structural changes giving rise to enhanced electron scattering to low angles, as observed in the experiments. The STEM images were simulated using QSTEM,[40] and simulation parameters were chosen to approximate the experimental conditions (refer to Experimental and Calculation Details section). Each energetically relaxed structure was repeated to create a supercell structure of 15 nm thickness along the electron beam direction (refer to the Supporting Information). The simulated STEM−ADF images are presented in Figure 5e−h for structures SI, SII, SIII, and SIV, respectively (simulated STEM−HAADF images are given in Figure S5 in the Supporting Information). By careful inspection, a variation in intensity can be recognized in Figure 5e,h. The corresponding intensity profiles across the simulated regions are plotted in Figure 5i. This demonstrates that the simulated STEM−ADF image intensities of structures SI, SII, and SIII are substantially comparable. On the other hand, the intensity profile of the simulated STEM−ADF image of structures SI and SIV differs significantly.

The calculated mean image intensities, I_{mean}, of the corresponding simulated STEM−ADF images are as follows: $(I_{mean} = 138)_{SI} > (I_{mean} = 135)_{SII} > (I_{mean} = 133)_{SIII} > (I_{mean} = 122)_{SIV}$. The simulated ADF image of structure SIV shows a significant decrease in intensity with respect to that for SI. The calculated intensity ratios (1.13) of the simultaneous ADF signals of structure SI and structure SIV are remarkably equivalent to the computed intensity ratios (1.10) of the two sites (where the contrast fluctuates) of the experimental STEM−ADF image. These results clearly demonstrate that the cumulative effect of both O vacancies (including the accompanied lattice relaxations) and Mn-ion (B-site) displacements are contrasting in the experimental STEM−ADF image.

4. CONCLUSIONS

To summarize, we provide a thorough structural characterization by resorting to (S)TEM imaging, GPA, EELS, and EDX analysis, as well as DFT and multislice calculations. The experimental data show the presence of a 7 nm-thick interfacial region in the LSMO film, commonly associated with the formation of a magnetic dead layer at the film/substrate interface, with structural and electronic properties that are clearly different from the rest of the film. STEM−ADF imaging and EELS analysis confirm the presence of oxygen vacancies in the LSMO films, with increasing concentration as nearing the film/substrate interface. In the same interfacial region, STEM−HAADF imaging also reveals that Mn ions are displaced by an amount of 29 pm ± 10 pm from their centrosymmetric positions. The existence of oxygen vacancies within the film region concurs to determine these lattice distortions, resulting in a lattice strain gradient, as also supported by GPA strain analysis performed on HRTEM images. We have emphasized the defect contrast due to the cumulative effect of Mn-ion displacement and oxygen vacancies within the interfacial layer using STEM−ADF imaging instead of only the use of STEM−HAADF image, which is most commonly used for thin-film characterization. Finally, DFT calculations and STEM image simulation support the experimental findings, enlightening that Mn-ion relocation is connected to the lowering of the Mn valence state at the film/substrate interface. Our findings result from the simultaneous acquisition of STEM−ADF and STEM−HAADF images, which has the key advantage of adding sensitivity to defects connected to light elements such as oxygen. We provide unprecedented evidence that the lowering of structural symmetry due to Mn-ion displacement is linked to the Mn valence state reduction at the interfacial region, thus opening new perspectives on the possibility to tune the magnetic anisotropy of LSMO thin films via a strain-driven thin-film technology.

■ ASSOCIATED CONTENT

Supporting Information

The Supporting Information is available free of charge at https://pubs.acs.org/doi/10.1021/acsami.1c15599.

t/λ map using the EELS spectra; strain map calculated from the STEM−HAADF image; chemical composition analysis using EDXS; determination of the Mn valence state; quantification of Mn-ion (B-site) displacements; details of DFT calculations; and STEM image simulation (PDF)

■ AUTHOR INFORMATION

Corresponding Authors

Piu Rajak − *Istituto Officina dei Materiali-CNR, 34149 Trieste, Italy;* orcid.org/0000-0002-8728-7459; Email: rajak@iom.cnr.it

Regina Ciancio − *Istituto Officina dei Materiali-CNR, 34149 Trieste, Italy;* orcid.org/0000-0003-1739-3763; Email: ciancio@iom.cnr.it

Authors

Daniel Knez − *Institute of Electron Microscopy and Nanoanalysis, Graz University of Technology, 8010 Graz, Austria;* orcid.org/0000-0003-0755-958X

Sandeep Kumar Chaluvadi − *Istituto Officina dei Materiali-CNR, 34149 Trieste, Italy;* orcid.org/0000-0002-3689-3336

Pasquale Orgiani − *Istituto Officina dei Materiali-CNR, 34149 Trieste, Italy; CNR-SPIN, UOS Salerno, 84084 Fisciano, Salerno, Italy;* orcid.org/0000-0002-1082-9651

Giorgio Rossi − *Istituto Officina dei Materiali-CNR, 34149 Trieste, Italy; Dipartimento di Fisica, Università degli Studi di Milano, 20133 Milano, Italy;* orcid.org/0000-0002-9330-7436

Laurence Méchin − *Normandie University, UNICAEN, ENSICAEN, CNRS, GREYC, 14000 Caen, France;* orcid.org/0000-0002-6350-1801

Complete contact information is available at: https://pubs.acs.org/10.1021/acsami.1c15599

Author Contributions

P.R., D.K., and R.C. conceived the experiment. D.K., P.R., and R.C. performed the TEM experiments. D.K. performed the TEM/EELS experiments by an aberration-corrected microscope. P.R. carried out data analysis, GPA, and theoretical calculations. S.K.C., P.O., and L.M. grew the films and performed structural characterization by XRD. G.R. contributed to the discussion of the results and to review drafts.

https://doi.org/10.1021/acsami.1c15599
ACS Appl. Mater. Interfaces 2021, 13, 55666−55675

P.R. and R.C. wrote the paper with the contribution from all the authors.

Notes

The authors declare no competing financial interest.

■ ACKNOWLEDGMENTS

This work has received funding from the EU-H2020 research and innovation programme under grant agreement no. 654360 having benefitted from the access provided by CNR-IOM in Trieste within the framework of the NFFA-Europe Transnational Access Activity (proposal ID334) and performed in the framework of the Nanoscience Foundry and Fine Analysis (NFFA-MIUR Italy Progetti Internazionali) facility. Advanced TEM experiments have been performed under the support of the European Union's Horizon 2020 research and innovation programme under grant agreement no. 823717-ESTEEM3. E. Cociancich is gratefully acknowledged for the TEM specimen preparation. P.R. acknowledges the receipt of a fellowship from the ICTP Programme for Training and Research in Italian Laboratories, Trieste, Italy. D.K. acknowledges the financial support by the "Zukunftsfonds Steiermark" for funding of the K2 camera.

■ REFERENCES

(1) Urushibara, A.; Moritomo, Y.; Arima, T.; Asamitsu, A.; Kido, G.; Tokura, Y. Insulator-Metal Transition and Giant Magnetoresistance in $La_{1-X}Sr_xMnO_3$. *Phys. Rev. B: Condens. Matter Mater. Phys.* **1995**, *51*, 14103−14109.

(2) Tokura, Y.; Tomioka, Y. Colossal Magnetoresistive Manganites. *J. Magn. Magn. Mater.* **1999**, *200*, 1−23.

(3) Schiffer, P.; Ramirez, A. P.; Bao, W.; Cheong, S.-W. Low Temperature Magnetoresistance and the Magnetic Phase Diagram of $La_{1-X}Ca_xMnO_3$. *Phys. Rev. Lett.* **1995**, *75*, 3336−3339.

(4) Mitchell, J. F.; Argyriou, D. N.; Berger, A.; Gray, K. E.; Osborn, R.; Welp, U. Spin, Charge, and Lattice States in Layered Magnetoresistive Oxides. *J. Phys. Chem. B* **2001**, *105*, 10731−10745.

(5) Salamon, M. B.; Jaime, M. The Physics of Manganites: Structure and Transport. *Rev. Mod. Phys.* **2001**, *73*, 583−628.

(6) Israel, C.; Calderón, M. J.; Mathur, N. D. The Current Spin on Manganites. *Mater. Today* **2007**, *10*, 24−32.

(7) Li, Q. A.; Gray, K. E.; Zheng, H.; Claus, H.; Rosenkranz, S.; Ancona, S. N.; Osborn, R.; Mitchell, J. F.; Chen, Y.; Lynn, J. W. Reentrant Orbital Order and the True Ground State of $LaSr_2Mn_2O_7$. *Phys. Rev. Lett.* **2007**, *98*, 167201.

(8) Bonn, D. A. Are High-Temperature Superconductors Exotic? *Nat. Phys.* **2006**, *2*, 159−168.

(9) Zheng, H.; Li, Q. A.; Gray, K. E.; Mitchell, J. F. Charge and Orbital Ordered Phases of $La_{2-2x}Sr_{1+2x}Mn_2O_{7-\delta}$. *Phys. Rev. B: Condens. Matter Mater. Phys.* **2008**, *78*, 155103.

(10) Huijben, M.; Martin, L. W.; Chu, Y.-H.; Holcomb, M. B.; Yu, P.; Rijnders, G.; Blank, D. H. A.; Ramesh, R. Critical Thickness and Orbital Ordering in Ultrathin $La_{0.7}Sr_{0.3}MnO_3$ Films. *Phys. Rev. B: Condens. Matter Mater. Phys.* **2008**, *78*, 094413.

(11) Sun, J. Z.; Abraham, D. W.; Rao, R. A.; Eom, C. B. Thickness Dependent Magnetotransport in Ultra-Thin Manganite Films. *Appl. Phys. Lett.* **1998**, *74*, 3017−3019.

(12) Borges, R. P.; Guichard, W.; Lunney, J. G.; Coey, J. M. D.; Ott, F. Magnetic and Electric "Dead" Layers in $(La_{0.7}Sr_{0.3})MnO_3$ Thin Films. *J. Appl. Phys.* **2001**, *89*, 3868−3873.

(13) Liao, Z.; Li, F.; Gao, P.; Li, L.; Guo, J.; Pan, X.; Jin, R.; Plummer, E. W.; Zhang, J. Origin of the Metal-Insulator Transition in Ultrathin Films of $La_{2/3}Sr_{1/3}MnO_3$. *Phys. Rev. B: Condens. Matter Mater. Phys.* **2015**, *92*, 125123.

(14) Kourkoutis, L. F.; Song, J. H.; Hwang, H. Y.; Muller, D. A. Microscopic Origins for Stabilizing Room-Temperature Ferromagnetism in Ultrathin Manganite Layers. *Proc. Natl. Acad. Sci. U.S.A.* **2010**, *107*, 11682−11685.

(15) Izumi, M.; Ogimoto, Y.; Manako, T.; Kawasaki, M.; Tokura, Y. Interface Effect and Its Doping Dependence in $La_{1-X}Sr_XMnO_3$/$SrTiO_3$ Superlattices. *J. Phys. Soc. Jpn.* **2002**, *71*, 2621−2624.

(16) Tebano, A.; Aruta, C.; Sanna, S.; Medaglia, P. G.; Balestrino, G.; Sidorenko, A. A.; De Renzi, R.; Ghiringhelli, G.; Braicovich, L.; Bisogni, V.; Brookes, N. B. Evidence of Orbital Reconstruction at Interfaces in Ultrathin $La_{0.7}Sr_{0.3}MnO_3$ Films. *Phys. Rev. Lett.* **2008**, *100*, 137401.

(17) Li, X.; Lindfors-Vrejoiu, I.; Ziese, M.; Gloter, A.; van Aken, P. A. Impact of Interfacial Coupling of Oxygen Octahedra on Ferromagnetic Order in $La_{0.7}Sr_{0.3}MnO_3/SrTiO_3$ Heterostructures. *Sci. Rep.* **2017**, *7*, 40068.

(18) Liao, Z.; Huijben, M.; Zhong, Z.; Gauquelin, N.; Macke, S.; Green, R. J.; Van Aert, S.; Verbeeck, J.; Van Tendeloo, G.; Held, K.; Sawatzky, G. A.; Koster, G.; Rijnders, G. Controlled Lateral Anisotropy in Correlated Manganite Heterostructures by Interface-Engineered Oxygen Octahedral Coupling. *Nat. Mater.* **2016**, *15*, 425−431.

(19) Ishii, Y.; Yamada, H.; Sato, H.; Akoh, H.; Ogawa, Y.; Kawasaki, M.; Tokura, Y. Improved Tunneling Magnetoresistance in Interface Engineered $(La,Sr)MnO_3$ Junctions. *Appl. Phys. Lett.* **2006**, *89*, 042509.

(20) Matou, T.; Takeshima, K.; Anh, L. D.; Seki, M.; Tabata, H.; Tanaka, M.; Ohya, S. Reduction of the Magnetic Dead Layer and Observation of Tunneling Magnetoresistance in $La_{0.67}$ $Sr_{0.33}MnO_3$ -Based Heterostructures with a $LaMnO_3$ Layer. *Appl. Phys. Lett.* **2017**, *110*, 212406.

(21) Boschker, H.; Verbeeck, J.; Egoavil, R.; Bals, S.; Van Tendeloo, G.; Huijben, M.; Houwman, E. P.; Koster, G.; Blank, D. H. A.; Rijnders, G. Preventing the Reconstruction of the Polar Discontinuity at Oxide Heterointerfaces. *Adv. Funct. Mater.* **2012**, *22*, 2235−2240.

(22) Peng, R.; Xu, H. C.; Xia, M.; Zhao, J. F.; Xie, X.; Xu, D. F.; Xie, B. P.; Feng, D. L. Tuning the Dead-Layer Behavior of $La_{0.67}Sr_{0.33}MnO_3/SrTiO_3$ via Interfacial Engineering. *Appl. Phys. Lett.* **2014**, *104*, 081606.

(23) Huijben, M.; Liu, Y.; Boschker, H.; Lauter, V.; Egoavil, R.; Verbeeck, J.; te Velthuis, S. G. E.; Rijnders, G.; Koster, G. Enhanced Local Magnetization by Interface Engineering in Perovskite-Type Correlated Oxide Heterostructures. *Adv. Mater. Interfaces* **2015**, *2*, 1400416.

(24) Glazer, A. M. The Classification of Tilted Octahedra in Perovskites. *Acta Crystallogr., Sect. B: Struct. Crystallogr. Cryst. Chem.* **1972**, *28*, 3384−3392.

(25) Kan, D.; Aso, R.; Sato, R.; Haruta, M.; Kurata, H.; Shimakawa, Y. Tuning Magnetic Anisotropy by Interfacially Engineering the Oxygen Coordination Environment in a Transition Metal Oxide. *Nat. Mater.* **2016**, *15*, 432−437.

(26) Adamo, C.; Ke, X.; Wang, H. Q.; Xin, H. L.; Heeg, T.; Hawley, M. E.; Zander, W.; Schubert, J.; Schiffer, P.; Muller, D. A.; Maritato, L.; Schlom, D. G. Effect of Biaxial Strain on the Electrical and Magnetic Properties of (001) $La_{0.7}Sr_{0.3}MnO_3$ Thin Films. *Appl. Phys. Lett.* **2009**, *95*, 112504.

(27) Boschker, H.; Mathews, M.; Houwman, E. P.; Nishikawa, H.; Vailionis, A.; Koster, G.; Rijnders, G.; Blank, D. H. A. Strong Uniaxial In-Plane Magnetic Anisotropy of (001)- and (011)-Oriented $La_{0.67}Sr_{0.33}MnO_3$ Thin Films on $NdGaO_3$ Substrates. *Phys. Rev. B: Condens. Matter Mater. Phys.* **2009**, *79*, 214425.

(28) Cao, L.; Petracic, O.; Zakalek, P.; Weber, A.; Rücker, U.; Schubert, J.; Koutsioubas, A.; Mattauch, S.; Brückel, T. Reversible Control of Physical Properties via an Oxygen-Vacancy-Driven Topotactic Transition in Epitaxial $La_{0.7}Sr_{0.3}MnO_{3-\delta}$ Thin Films. *Adv. Mater.* **2019**, *31*, 1806183.

(29) Tan, H.; Verbeeck, J.; Abakumov, A.; Van Tendeloo, G. Oxidation State and Chemical Shift Investigation in Transition Metal Oxides by EELS. *Ultramicroscopy* **2012**, *116*, 24−33.

(30) Varela, M.; Oxley, M. P.; Luo, W.; Tao, J.; Watanabe, M.; Lupini, A. R.; Pantelides, S. T.; Pennycook, S. J. Atomic-Resolution

https://doi.org/10.1021/acsami.1c15599
ACS Appl. Mater. Interfaces 2021, 13, 55666−55675

Imaging of Oxidation States in Manganites. *Phys. Rev. B: Condens. Matter Mater. Phys.* **2009**, *79*, 085117.
(31) Li, Z.; Bosman, M.; Yang, Z.; Ren, P.; Wang, L.; Cao, L.; Yu, X.; Ke, C.; Breese, M. B. H.; Rusydi, A.; Zhu, W.; Dong, Z.; Foo, Y. L. Interface and Surface Cation Stoichiometry Modified by Oxygen Vacancies in Epitaxial Manganite Films. *Adv. Funct. Mater.* **2012**, *22*, 4312−4321.
(32) Kurata, H.; Colliex, C. Electron-Energy-Loss Core-Edge Structures in Manganese Oxides. *Phys. Rev. B: Condens. Matter Mater. Phys.* **1993**, *48*, 2102−2108.
(33) Wang, Z. L.; Yin, J. S.; Jiang, Y. D.; Zhang, J. Studies of Mn Valence Conversion and Oxygen Vacancies in $La_{1-x}Ca_xMnO_{3-y}$ Using Electron Energy-Loss Spectroscopy. *Appl. Phys. Lett.* **1997**, *70*, 3362−3364.
(34) Krivanek, O. L.; Disko, M. M.; Taftø, J.; Spence, J. C. H. Electron Energy Loss Spectroscopy as a Probe of the Local Atomic Environment. *Ultramicroscopy* **1982**, *9*, 249−254.
(35) Jin, L.; Jia, C.-L.; Lindfors-Vrejoiu, I.; Zhong, X.; Du, H.; Dunin-Borkowski, R. E. Direct Demonstration of a Magnetic Dead Layer Resulting from A-Site Cation Inhomogeneity in a $(La,Sr)MnO_3$ Epitaxial Film System. *Adv. Mater. Interfaces* **2016**, *3*, 1600414.
(36) Hÿtch, M. J.; Snoeck, E.; Kilaas, R. Quantitative Measurement of Displacement and Strain Fields from HREM Micrographs. *Ultramicroscopy* **1998**, *74*, 131−146.
(37) Chaluvadi, S. K.; Ajejas, F.; Orgiani, P.; Lebargy, S.; Minj, A.; Flament, S.; Camarero, J.; Perna, P.; Méchin, L. Epitaxial Strain and Thickness Dependent Structural, Electrical and Magnetic Properties of $La_{0.67}Sr_{0.33}MnO_3$ Films. *J. Phys. D: Appl. Phys.* **2020**, *53*, 375005.
(38) Egerton, R. F. *Electron Energy-Loss Spectroscopy in the Electron Microscope*, 2nd ed.; Plenum Press: New York, 1996.
(39) De Backer, A.; van den Bos, K. H. W.; Van den Broek, W.; Sijbers, J.; Van Aert, S. StatSTEM: An Efficient Approach for Accurate and Precise Model-Based Quantification of Atomic Resolution Electron Microscopy Images. *Ultramicroscopy* **2016**, *171*, 104−116.
(40) Koch, C. T. *Determination of Core Structure Periodicity and Point Defect Density along Dislocations*; Arizona State University, 2002.
(41) Giannozzi, P.; Baroni, S.; Bonini, N.; Calandra, M.; Car, R.; Cavazzoni, C.; Ceresoli, D.; Chiarotti, G. L.; Cococcioni, M.; Dabo, I.; Dal Corso, A.; De Gironcoli, S.; Fabris, S.; Fratesi, G.; Gebauer, R.; Gerstmann, U.; Gougoussis, C.; Kokalj, A.; Lazzeri, M.; Martin-Samos, L.; Marzari, N.; Mauri, F.; Mazzarello, R.; Paolini, S.; Pasquarello, A.; Paulatto, L.; Sbraccia, C.; Scandolo, S.; Sclauzero, G.; Seitsonen, A. P.; Smogunov, A.; Umari, P.; Wentzcovitch, R. M. QUANTUM ESPRESSO: A Modular and Open-Source Software Project for Quantum Simulations of Materials. *J. Phys.: Condens. Matter* **2009**, *21*, 395502.
(42) Perdew, J. P.; Burke, K.; Ernzerhof, M. Generalized Gradient Approximation Made Simple. *Phys. Rev. Lett.* **1996**, *77*, 3865−3868.
(43) Kresse, G.; Joubert, D. From Ultrasoft Pseudopotentials to the Projector Augmented-Wave Method. *Phys. Rev. B: Condens. Matter Mater. Phys.* **1999**, *59*, 1758−1775.
(44) Guzmán, R.; Maurel, L.; Langenberg, E.; Lupini, A. R.; Algarabel, P. A.; Pardo, J. A.; Magén, C. Polar-Graded Multiferroic $SrMnO_3$ Thin Films. *Nano Lett.* **2016**, *16*, 2221−2227.
(45) Radaelli, P. G.; Iannone, G.; Marezio, M.; Hwang, H. Y.; Cheong, S.-W.; Jorgensen, J. D.; Argyriou, D. N. Structural Effects on the Magnetic and Transport Properties of Perovskite $A_{1-X}A'_xMnO_3$ (X=0.25, 0.30). *Phys. Rev. B: Condens. Matter Mater. Phys.* **1997**, *56*, 8265−8276.
(46) Vailionis, A.; Boschker, H.; Siemons, W.; Houwman, E. P.; Blank, D. H. A.; Rijnders, G.; Koster, G. Misfit Strain Accommodation in Epitaxial ABO_3 Perovskites: Lattice Rotations and Lattice Modulations. *Phys. Rev. B: Condens. Matter Mater. Phys.* **2011**, *83*, 1−10.
(47) Vailionis, A.; Boschker, H.; Liao, Z.; Smit, J. R. A.; Rijnders, G.; Huijben, M.; Koster, G. Symmetry and Lattice Mismatch Induced Strain Accommodation near and Away from Correlated Perovskite Interfaces. *Appl. Phys. Lett.* **2014**, *105*, 131906.
(48) Howie, A. Image Contrast and Localized Signal Selection Techniques. *J. Microsc.* **1979**, *117*, 11−23.
(49) Kirkland, E. J.; Loane, R. F.; Silcox, J. Simulation of Annular Dark Field STEM Images Using a Modified Multislice Method. *Ultramicroscopy* **1987**, *23*, 77−96.
(50) Muller, D. A.; Nakagawa, N.; Ohtomo, A.; Grazul, J. L.; Hwang, H. Y. Atomic-Scale Imaging of Nanoengineered Oxygen Vacancy Profiles in $SrTiO_3$. *Nature* **2004**, *430*, 657−661.
(51) Johnston-Peck, A. C.; Winterstein, J. P.; Roberts, A. D.; DuChene, J. S.; Qian, K.; Sweeny, B. C.; Wei, W. D.; Sharma, R.; Stach, E. A.; Herzing, A. A. Oxidation-State Sensitive Imaging of Cerium Dioxide by Atomic-Resolution Low-Angle Annular Dark Field Scanning Transmission Electron Microscopy. *Ultramicroscopy* **2016**, *162*, 52−60.
(52) Angeloni, M.; Balestrino, G.; Boggio, N. G.; Medaglia, P. G.; Orgiani, P.; Tebano, A. Suppression of the Metal-Insulator Transition Temperature in Thin $La_{0.7}Sr_{0.3}MnO_3$ Films. *J. Appl. Phys.* **2004**, *96*, 6387−6392.
(53) Hillyard, S.; Silcox, J. Detector Geometry, Thermal Diffuse Scattering and Strain Effects in ADF STEM Imaging. *Ultramicroscopy* **1995**, *58*, 6−17.
(54) Perovic, D. D.; Rossouw, C. J.; Howie, A. Imaging Elastic Strains in High-Angle Annular Dark Field Scanning Transmission Electron Microscopy. *Ultramicroscopy* **1993**, *52*, 353−359.
(55) Phillips, P. J.; De Graef, M.; Kovarik, L.; Agrawal, A.; Windl, W.; Mills, M. J. Atomic-Resolution Defect Contrast in Low Angle Annular Dark-Field STEM. *Ultramicroscopy* **2012**, *116*, 47−55.
(56) Plamann, T.; Hÿtch, M. J. Tests on the Validity of the Atomic Column Approximation for STEM Probe Propagation. *Ultramicroscopy* **1999**, *78*, 153−161.
(57) Cowley, J. M.; Huang, Y. De-Channelling Contrast in Annular Dark-Field STEM. *Ultramicroscopy* **1992**, *40*, 171−180.
(58) Yao, L.; Majumdar, S.; Äkäslompolo, L.; Inkinen, S.; Qin, Q. H.; Van Dijken, S. Electron-Beam-Induced Perovskite-Brownmillerite-Perovskite Structural Phase Transitions in Epitaxial $La_{2/3}Sr_{1/3}MnO_3$ Films. *Adv. Mater.* **2014**, *26*, 2789−2793.
(59) Hemberger, J.; Krimmel, A.; Kurz, T.; Krug von Nidda, H. A.; Ivanov, V. Y.; Mukhin, A. A.; Balbashov, A. M.; Loidl, A. Structural, Magnetic, and Electrical Properties of Single-Crystalline $La_{1-X}Sr_xMnO_3$ ($0.4<x<0.85$). *Phys. Rev. B: Condens. Matter Mater. Phys.* **2002**, *66*, 094410.
(60) Liao, Z.; Zhang, J. Metal-to-Insulator Transition in Ultrathin Manganite Heterostructures. *Appl. Sci.* **2019**, *9*, 144.
(61) Kobrinskii, A. L.; Goldman, A. M.; Varela, M.; Pennycook, S. J. Thickness Dependence of the Exchange Bias in Epitaxial Manganite Bilayers. *Phys. Rev. B: Condens. Matter Mater. Phys.* **2009**, *79*, 094405.
(62) Venkatesan, S.; Döblinger, M.; Daumont, C.; Kooi, B.; Noheda, B.; De Hosson, J. T. M.; Scheu, C. Influence of Strain on the Electronic Structure of the $TbMnO_3/SrTiO_3$ Epitaxial Interface. *Appl. Phys. Lett.* **2011**, *99*, 222902.
(63) Orgiani, P.; Galdi, A.; Aruta, C.; Cataudella, V.; De Filippis, G.; Perroni, C. A.; Marigliano Ramaglia, V.; Ciancio, R.; Brookes, N. B.; Moretti Sala, M.; Ghiringhelli, G.; Maritato, L. Multiple Double-Exchange Mechanism by Mn^{2+} Doping in Manganite Compounds. *Phys. Rev. B: Condens. Matter Mater. Phys.* **2010**, *82*, 205122.
(64) Penn, A. N.; Koohfar, S.; Kumah, D. P.; Lebeau, J. M. On the Redistribution of Charge in $La_{0.7}Sr_{0.3}CrO_3/La_{0.7}Sr_{0.3}MnO_3$ Multilayer Thin Films. *AIP Adv.* **2020**, *10*, 045133.
(65) Ko, E. K.; Mun, J.; Lee, H. G.; Kim, J.; Song, J.; Chang, S. H.; Kim, T. H.; Chung, S. B.; Kim, M.; Wang, L.; Noh, T. W. Oxygen Vacancy Engineering for Highly Tunable Ferromagnetic Properties: A Case of $SrRuO_3$ Ultrathin Film with a $SrTiO_3$ Capping Layer. *Adv. Funct. Mater.* **2020**, *30*, 2001486.
(66) Lu, J.; Si, L.; Yao, X.; Tian, C.; Wang, J.; Zhang, Q.; Lai, Z.; Malik, I. A.; Liu, X.; Jiang, P.; Zhu, K.; Shi, Y.; Luo, Z.; Gu, L.; Held, K.; Mi, W.; Zhong, Z.; Nan, C.-W.; Zhang, J. Electric Field Controllable High-Spin $SrRuO_3$ Driven by a Solid Ionic Junction. *Phys. Rev. B* **2020**, *101*, 214401.

https://doi.org/10.1021/acsami.1c15599
ACS Appl. Mater. Interfaces 2021, 13, 55666−55675

(67) Yang, N.; Orgiani, P.; Di Bartolomeo, E.; Foglietti, V.; Torelli, P.; Ievlev, A. V.; Rossi, G.; Licoccia, S.; Balestrino, G.; Kalinin, S. V.; Aruta, C. Effects of Dopant Ionic Radius on Cerium Reduction in Epitaxial Cerium Oxide Thin Films. *J. Phys. Chem. C* **2017**, *121*, 8841−8849.
(68) von Harrach, H. S. Instrumental Factors in High-Resolution FEG STEM. *Ultramicroscopy* **1995**, *58*, 1−5.
(69) Qiao, Q.; Zhang, Y.; Contreras-Guerrero, R.; Droopad, R.; Pantelides, S. T.; Pennycook, S. J.; Ogut, S.; Klie, R. F. Direct Observation of Oxygen-Vacancy-Enhanced Polarization in a $SrTiO_3$-Buffered Ferroelectric $BaTiO_3$ Film on GaAs. *Appl. Phys. Lett.* **2015**, *107*, 201604.

https://doi.org/10.1021/acsami.1c15599
ACS Appl. Mater. Interfaces 2021, 13, 55666−55675